Equatorial waves in High Resolution Dynamics Limb Sounder (HIRDLS) data

M. J. Alexander[1] and D. A. Ortland[2]

[1]   We examine equatorial wave structure in temperature measurements from the High Resolution Dynamics Limb Sounder (HIRDLS) on the Aura satellite. Waves with periods longer than 1 day and zonal wave numbers up to 8 (depending on frequency) are derived from an asynoptic Fourier transform analysis. HIRDLS measurement sampling and resolution afford unprecedented views of the latitude-height structure of equatorial Rossby wave, mixed Rossby-gravity wave, and Kelvin wave modes at altitudes above cloud tops in the tropical upper troposphere and stratosphere. Wave modes with vertical wavelength as short as 4 km can be clearly seen in the data. Kelvin waves comprise a dominant signal throughout the 3 years of HIRDLS measurements, and we further examine time, height, and longitude variations observed in the Kelvin waves. An annual cycle of Kelvin wave temperature amplitudes near the tropopause is observed that may have implications for annual variations in wave-cirrus formation in the tropics. This annual variation can be largely explained by effects of the background wind and stability on Kelvin wave propagation and potential energy in the tropical tropopause layer. At altitudes 20 km and above, the annual cycle gives way to an interannual cycle in Kelvin wave amplitudes that is related to the quasi-biennial oscillation in stratospheric winds. This interannual variation is a signature of Kelvin wave forcing of the descent of westerly winds in the oscillation, and we compute the Kelvin wave fractional contribution to the forcing.

1.   Introduction

[2]   Equatorial waves forced by tropical convection drive the quasi-biennial oscillation (QBO) in lower stratospheric winds and contribute to driving semiannual oscillations in the winds at higher altitudes [*Holton*, 1972; *Giorgetta et al.*, 2002; *Kawatani et al.*, 2010; *Garcia et al.*, 1997; *Sassi and Garcia*, 1997]. Circulation responses to equatorial waves may also be important for transport of trace constituents and water vapor in the tropopause transition layer (TTL) [*Boehm and Lee*, 2003; *Norton*, 2006; *Fueglistaler et al.*, 2009; *Ryu and Lee*, 2010]. Kelvin waves have been observed to play a role in the formation and modulation of tropical cirrus clouds [*Boehm and Verlinde*, 2000; *Fujiwara et al.*, 2009] and may play an important role in tropical cirrus occurrence frequencies [*Jensen and Pfister*, 2004] and stratospheric water vapor concentrations through their modulation of the tropical cold-point tropopause [*Tsuda et al.*, 1994; *Ryu et al.*, 2008]. Equatorial waves in the troposphere also serve to organize tropical convection as evidenced by the wave signatures in the space-time spectrum of tropical clouds [*Wheeler and Kiladis*, 1999; *Kiladis et al.*, 2009].

[3]   Satellite observations provide global coverage for characterization of equatorial waves. Early satellite data provided only coarse vertical and horizontal resolution, but identified Kelvin wave modes with deep vertical structure [*Salby et al.*, 1984; *Canziani et al.*, 1994, 1995; *Shiotani et al.*, 1997; *Srikanth and Ortland*, 1998]. Several recent studies have analyzed the properties of stratospheric equatorial waves in global positioning system (GPS) temperatures [*Tsai et al.*, 2004; *Randel and Wu*, 2005; *Alexander et al.*, 2008] and in SABER (Sounding of the Atmosphere using Broadband Emission Radiometry) temperatures [*Ern et al.*, 2008]. *Randel and Wu* [2005], using the limited set of GPS measurements available at the time, analyzed temperatures between 10 and 32 km, and identified Kelvin waves with zonal wave numbers $k = 1$ and 2 using data averaged over the latitudes 10°S–10°N. More recently, *Alexander et al.* [2008] using a larger set of GPS measurements resolved tropical waves up to $k = 9$ and described Kelvin waves up to $k = 5$ in an analysis using 10° latitude resolution. *Ern et al.* [2008] analyzed SABER data at 4° latitude resolution at altitudes above 20 km, and found Kelvin waves, equatorial Rossby (ER) waves, and mixed Rossby-gravity (MRG) waves in 31 day samples, and examined variations with QBO winds during a 4 year period. From SABER, *Ern and Preusse* [2009] also estimated the Kelvin wave contribution to QBO wind driving.

---

[1]CoRA Division/NorthWest Research Associates, Boulder, Colorado, USA.
[2]Seattle Division/NorthWest Research Associates, Redmond, Washington, USA.

[4] Temperature measurements from the High Resolution Dynamics Limb Sounder (HIRDLS) are capable of observing the three-dimensional and time-varying properties of equatorial waves at high vertical and latitudinal resolution. HIRDLS is a limb-scanning instrument on the Aura satellite that orbits in the international A-Train satellite constellation at high inclination in a Sun-synchronous orbit [*Gille et al.*, 2008]. A vertical field of view projection at the limb of only 1.2 km and vertical oversampling provide the high resolution necessary to observe the broad range of equatorial wave vertical wavelengths, which have been observed to be as short as 3–4.5 km [*Holton et al.*, 2001]. A fast vertical scan rate permits close spacing between temperature profiles along the measurement track, giving very high latitudinal resolution near the equator. The vertical resolution of HIRDLS temperature measurements is comparable to temperatures derived from GPS radio occultation [*Gille et al.*, 2008], while the space-time sampling in the tropical region is much greater than GPS. Global coverage of HIRDLS measurements is obtained every 12 h at altitudes between cloud tops and 60 km. The resolution in latitude is approximately 1°, and over 650 profiles are obtained daily between 10°S and 10°N latitude. In contrast, GPS observations from both COSMIC and CHAMP combined still only provide approximately 200 profiles per day at these latitudes. The GPS sampling is approximately random, so that the resolutions in latitude and longitude are approximately equivalent. On average, profiles collected in a 12 h period near the equator are spaced ~8° apart. SABER has coarser vertical resolution ~2 km, and coarser latitude resolution of 3°. It samples ~200 profiles per day in the 10°S–10°N latitude band. HIRDLS may therefore be able to observe equatorial waves with shorter vertical wavelengths, and can more clearly define the latitudinal structure of equatorial waves than previous measurements.

[5] We will examine the spectrum of equatorial waves observed by HIRDLS as well as the latitudinal and vertical structure of the wave modes resolved. Using 3 years of measurements, we will also examine the sensitivity of the spectrum to the phase of the QBO. Kelvin waves are a dominant component of the spectrum, and we examine both seasonal and interannual variations observed in these waves and also estimate their effects on the zonal mean circulation in the lower stratosphere.

2. HIRDLS Temperature Observations

[6] We use version 5 HIRDLS temperatures in this study. Version 5 temperatures are very similar to previous versions, but with improvements in temporal coverage. The data we analyze here span the available 3 year data record January 2005 to January 2008. HIRDLS flies on the Aura satellite in a 98° inclination orbit, and it scans the limb at a 47° angle from the orbit track. Profiles are reported at ~0.75 km vertical resolution, although the effective resolution is ~1 km [*Gille et al.*, 2008]. Our analysis is conducted on the native pressure-altitude grid (henceforth referred to simply as "altitude" with the symbol z). HIRDLS data include a cloud detection algorithm. At and below any level identified as cloud, the reported values are the a priori temperatures because clouds are opaque to the infrared emissions that HIRDLS detects. We therefore treat data at and below the cloud level as missing. The number of these "missing" values

increases below the tropopause, contributing to increasing error (fewer measurements) at low altitudes. The a priori data may contain waves, so prior to the spectral analysis we fill missing values with the zonal and time mean temperature. Latitudes viewed by HIRDLS range from 65°S to 84°N. In the present analysis we focus on equatorial latitudes, but all latitudes are analyzed in the same way. Although the HIRDLS temperature measurements extend from cloud top to 60 km in altitude, we focus here on altitudes 15–35 km, including the QBO and the tropical tropopause layer.

3. Asynoptic Fourier Analysis

[7] We use the *Salby* [1982] method for asynoptically sampled satellite observations to derive temperature spectra as a function of zonal wave number k and frequency ω. At 2.5° latitude increments, HIRDLS temperature data are separated into ascending and descending time series as a function of height. The mean in each latitude bin determines the zonal mean as a function of height. We subtract time mean of the zonal mean from the temperature profiles to subsequently study the perturbations. The longitude and time series for a given number of days of measurements are interpolated to a regular grid. The interpolation fills small gaps and corrects for small irregularities in scan rate or position, etc. Longitude resolution is on average 24.72°, and the number of orbits per day is 14.56. At each altitude and latitude, we apply the asynoptic Fourier space-time analysis [*Salby*, 1982] to identify prominent equatorial modes in the $k - \omega$ domain. This method resolves ω lower than 1 day^{-1}, and $|k|$ up to 8 (depending on the frequency). The data are divided into 60 day periods with 30 day overlap. Each 60 day time series is windowed with a Hanning (cosine) taper after removal of the time mean zonal mean to ensure stationarity in time prior to the Fourier analysis. Reconstructed time series for each period can later be superimposed to produce a continuous record over the 3 year data period.

[8] The spectrum averaged over all 3 years is dominated by eastward propagating Kelvin waves in the lower stratosphere below 30 km. Spectral power in westward propagating waves in the ER band is second in importance. Dominant spectral features are also known to be sensitive to the phase of the QBO. To bring out weaker features in the spectrum and examine the dependence on QBO phase, we average spectra at different times/heights with positive shear in the equatorial zonal winds (dU/dz) separately from times/heights with negative shear. We use the entire 3 year period here and altitudes in the lower stratosphere between 15 and 32 km. Figure 1 shows the result. Eastward propagating waves are plotted as positive wave numbers, and westward as negative. Figure 1 (left) is the average spectrum at times and altitudes when $dU/dz > 0$ and zonal wind is less than 8 m s^{-1}. Figure 1 (right) is the spectrum averaged over times and altitudes when $dU/dz < 0$ and zonal wind is greater than -20 m s^{-1}. Black regions at the extreme k are not resolved by the Salby method applied to HIRDLS data. Low ω waves with $k = 0$ are also omitted because the diurnal migrating tide is aliased to this position in the spectrum.

[9] Eastward propagating Kelvin waves remain the dominant feature in both phases of the shear at $k = 1$–5 and $\omega = 0.05$–0.32 cy/d (periods 3–20 days). The dotted lines in Figure 1 (left) outline phase speeds ranging from 7 to 75 m s^{-1}
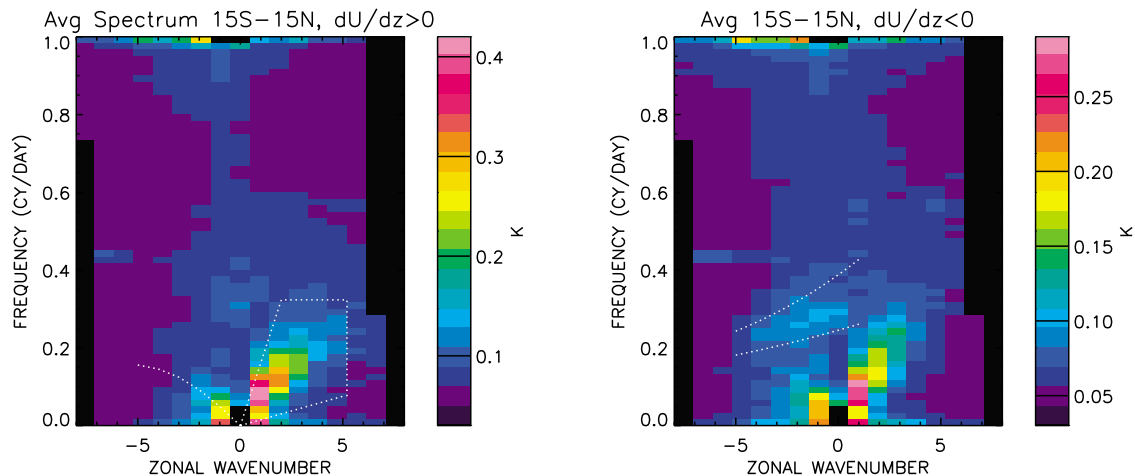
Figure 1. Temperature spectra averaged when zonal wind shear is (left) positive and (right) negative. Dotted white curves follow constant vertical wavelength dispersion curves for equatorial Rossby (ER), Kelvin, and mixed Rossby-gravity (MRG) waves as described in the text.

(equivalent to vertical wavelengths ~2–24 km) and the above k and ω limits for Kelvin waves. Westward propagating ER waves are also prominent in both phases at $k = -1$ and -2 and periods longer than ~10 days ($\omega = 0.1$ cy/d). The dispersion curve for ER waves with meridional mode $n = 1$ [*Matsuno*, 1966] and vertical wavelength 20 km is also shown. When shear is negative (descending easterly phase of the QBO), power in the westward propagating MRG wave band with k ranging −5 to 0 and periods ~3–4.5 days ($\omega = 0.23$–0.32 cy/d) becomes more apparent. The dotted lines on the right panel show dispersion curves for MRG waves with vertical wavelengths 4 and 10 km. We can also see a weak signal of eastward propagating inertia gravity waves with periods near 2 days in the spectra. Power at 1 day period will include nonmigrating tides forced by latent heating at the diurnal frequency.

[10] Figure 2 shows examples of equatorial wave modes identified in the asynoptic Fourier analysis. Figure 2 (left) shows a $k = -2$ mode with 4 day period in the MRG wave region of the spectrum. The tropical confinement and asymmetric structure across the equator with clear alternating positive and negative phase with height are remarkable given

that the analysis at each latitude/height point is completely independent of the others. The structure therefore confirms the interpretation of this mode as a MRG wave. We also note the very short vertical wavelength in this example, approximately 4 km, which is utilizing the full resolution of the HIRDLS measurements. Figure 4 (middle) shows the structure of the $k = -1$ mode with 20 day period that we interpret as a $n = 1$ ER wave mode with symmetric structure across the equator, largely confined to the lower stratosphere. Figure 4 (right) shows a Kelvin wave mode with $k = 1$ and 20 day period. Note these are only examples. Other modes or at other times can show much longer vertical wavelengths and/or deeper structure extending into the mesosphere.

[11] Figures 3 and 4 show examples of the latitude, height, and longitude structure of temperature filtered for the MRG wave band and ER wave bands, respectively, during periods of QBO westerly winds in the lower stratosphere. The MRG filter corresponds to westward waves with $k = 0$–5 and vertical wavelengths 4–10 km. Although the MRG waves appear weak in the averaged spectra in Figure 1, this is because they are more sporadic in occurrence than the slower waves, and they at times appear very clearly in the data. The character-
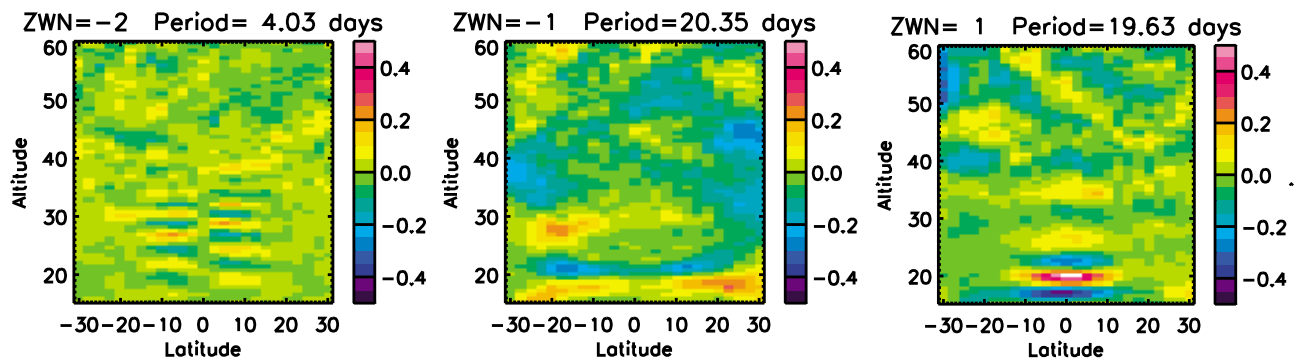

Figure 2. Examples of the latitude-height structure of equatorial wave modes identified by the asynoptic Fourier analysis of HIRDLS temperatures. The color scale is temperature (K). (left) MRG wave, (middle) ER wave, and (right) Kelvin wave modes. Each panel is labeled with the mode zonal wave number and period. The mode structures are clearest below ~35 km in these examples.
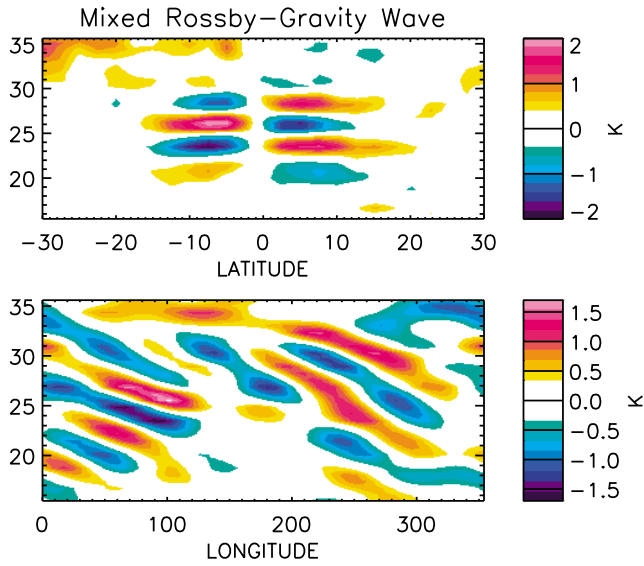
Figure 3. Structure of temperature signals filtered for MRG waves on day 305 in 2006. (top) Latitude height structure at 90° longitude. (bottom) Longitude height structure at −10° latitude.

istic equatorially trapped and antisymmetric structure across the equator of the MRG waves is very clearly resolved here. The ER wave filter includes westward k = 1–5, periods shorter than 32 days, and vertical wavelengths shorter than ~20 km. These transient ER waves display their characteristic symmetric structure. The 60 day window we have applied in the spectral analysis is not optimal for the nearly stationary ER waves, so we are only well-resolving the transient components here with periods shorter than ~30 days. The filtered results will include extratropical Rossby waves at higher latitudes. Figures 3 and 4 also show the MRG and ER phase
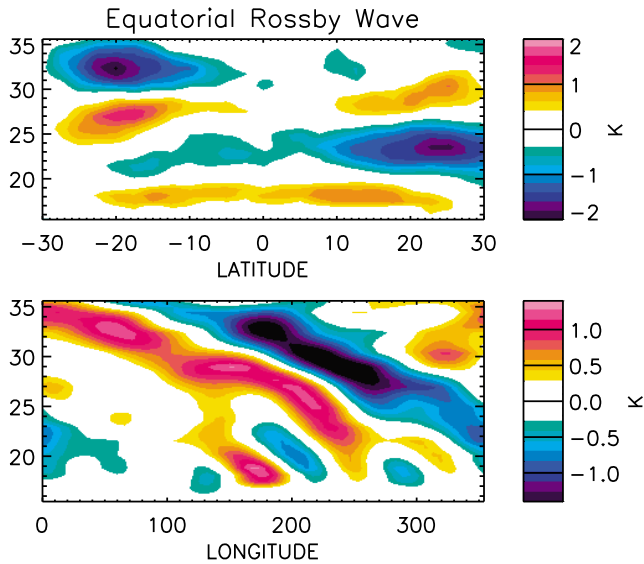
tilts westward with height, and in time series (not shown) both also show their westward propagation.

4. Kelvin Waves

[12] Strong signals in the Kelvin wave band are observed throughout the HIRDLS 3 year record. We next examine the Kelvin wave signals in the data throughout this period, January 2005 to January 2008. The Kelvin waves are isolated in $k - \omega$ space using the spectral limits: $1 \leq k \leq 5$, $.05 \leq \omega \leq 0.32$ cpd, $7 \leq c \leq 75$ m s^{-1}, where $c = \omega/k$ is Kelvin wave phase speed. Note that our filter would largely omit any power associated with the slow Madden-Julian oscillation [*Madden and Julian*, 1994]. After application of the Kelvin wave filter, the data are reconstructed as a function of latitude, longitude, height, and time.

4.1. Annual Cycle in the TTL

[13] Kelvin wave temperature fluctuations at the equator and at 16 km altitude are shown as a function of longitude and time in Figure 5. At this altitude, amplitudes reach ±2K and show a clear annual variation, with maximum values in the northern summer months between May and October. During these times, the largest amplitude oscillations tend to cluster in two longitude regions: Over the eastern hemisphere (including Africa, the Indian Ocean and western Pacific), and over the eastern Pacific. Although at times, particularly in 2006 and 2007, the perturbations are strong at all longitudes including the region of dateline. The annual cycle disappears by 20 km altitude, above which an interannual cycle dominates.
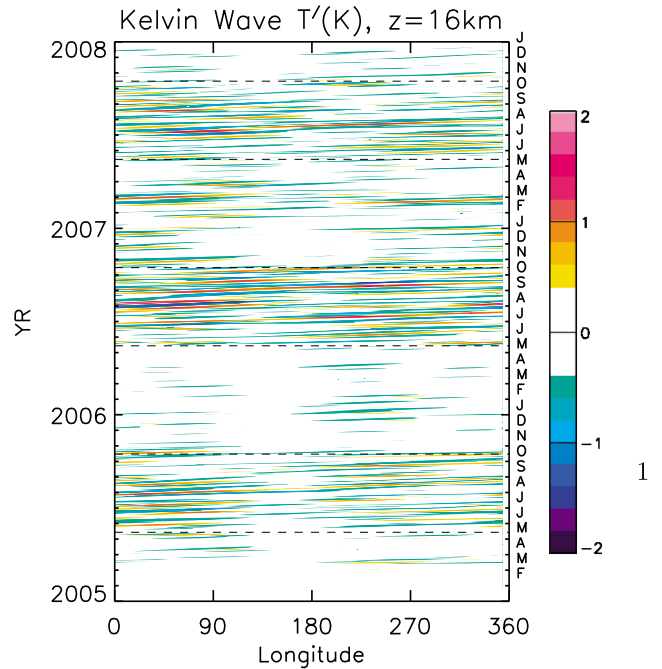

Figure 5. Temperature anomalies (K) at 16 km altitude at the equator associated with Kelvin waves as a function of longitude and time spanning the 3 years of measurements. The labels on the right indicate month of the year (e.g., F = February). Dashed lines mark the months of May and October.
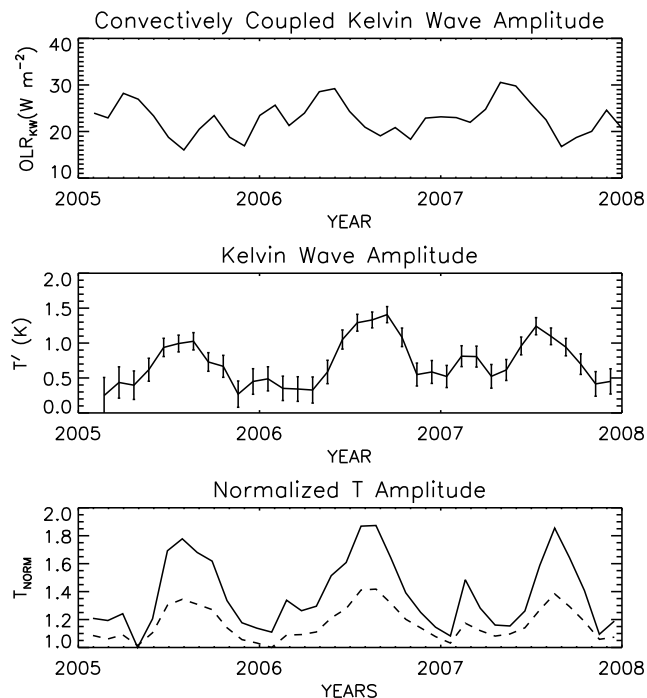

Figure 4. Structure of temperature signals filtered for ER waves on day 354 in 2006. (top) Latitude height structure at 186° longitude. (bottom) Longitude height structure at −15° latitude.

Figure 6. (top) OLR anomalies symmetric about the equator associated with Kelvin waves as a function time spanning the same period as in Figure 5. The values represent monthly means of the maximum amplitude occurring in longitude. (middle) Kelvin wave temperature amplitudes observed by HIRDLS at 16 km altitude, also shown as monthly means of the maximum values in longitude. (bottom) Time series of $\tilde{T}$ from (5) at 16 km altitude normalized by the minimum value. Two curves are shown, for 10 m s^{-1} (solid line) and 15 m s^{-1} (dashed line) phase speeds.

[14] One possibility for explaining this annual cycle would be a variation in Kelvin wave forcing. Tropical convection has pronounced annual cycles with the centers of maximum convection crossing back and forth across the equator about one month behind the latitude of zero solar zenith angle, but in the tropical latitudes the maximum following the equinox in March–April is much stronger than in September–October [*Meehl*, 1987; *Mitchell and Wallace*, 1992]. At periods and wave numbers associated with convectively coupled Kelvin waves, outgoing longwave radiation (OLR) and TRMM rainfall show a seasonal variation with maximum in northern winter (October to April) [*Cho et al.*, 2004], opposite to the annual cycle we observe in Kelvin waves in the TTL. Similarly, *Masunaga* [2007] found the maximum Kelvin wave signal in OLR on the equator in the March–April–May season.

[15] To compare the convectively coupled Kelvin wave signal to our stratospheric Kelvin waves more directly, we compute the band-pass filtered Kelvin wave OLR signal for the same 2005–2008 period covered by the HIRDLS data using the NOAA Interpolated OLR product [*Liebmann and Smith*, 1996]. We space-time Fourier analyze the symmetric component of 2.5° × 2.5° OLR data at latitudes 5°S–5°N. The same Kelvin wave filter previously applied for the HIRDLS temperature analysis is applied in the $k - \omega$ domain before transforming back to longitude-time. We then compute

monthly means of the maximum amplitude and show the results in Figure 6. Figure 6 (top) shows changes in time in this OLR Kelvin wave signal, which does not correspond well to the variations we observe in TTL Kelvin wave temperature amplitudes (Figure 6, middle). The convectively coupled waves peak ~April with minima ~August. The monthly mean in the maximum Kelvin wave amplitudes shown in Figure 6 (middle) varies from ~0.5 K or less from November through April to ~1–1.5 K in the June–August period. A previous multiyear analysis of GPS temperatures [*Alexander et al.*, 2008] did not specifically report an annual cycle in Kelvin wave amplitudes at these altitudes, but they did report a similar lack of correspondence between convectively coupled Kelvin waves in OLR data and Kelvin waves in GPS temperatures during a 6 month period in 2007. *Randel and Wu* [2005] saw largest TTL amplitudes for $k = 1$–2 Kelvin waves during December–February in GPS temperatures, but only examined a 14 month data record.

[16] Errors in the HIRDLS Kelvin wave temperature amplitudes are also shown in Figure 6 (middle), and these do display an annual cycle. Errors are smaller in boreal summer and larger in boreal winter, opposite to the Kelvin wave temperature amplitude cycle. The increase of noise in boreal winter is caused by the decrease in the number of available HIRDLS measurements (see section 2) due to the presence of cirrus clouds in the colder TTL conditions during this season [*Massie et al.*, 2010]. The noise increase is however only ~25–50% whereas the observed temperature amplitude increases by a factor of ~2. Selective data loss could potentially exaggerate the decrease in temperature amplitudes if larger amplitude waves preferentially induce cirrus formation, however this mechanism seems unlikely to fully account for the observed annual cycle in amplitudes since it is seen at altitudes as high as 18 km.

[17] Another explanation for the annual cycle at TTL altitudes involves changes in the Kelvin wave potential energy associated with changes in the background wind and stability. To examine this effect, we start by considering conservative propagation of Kelvin waves through the observed zonal mean zonal wind and static stability fields as given by the NCEP reanalysis. To isolate the effects of the background atmosphere, we examine the case where wave action A in the upper troposphere is constant in time. The assumption of constant A is chosen as a way to place the focus on how background wind and stability variations in time can affect Kelvin wave temperature amplitudes. For Kelvin waves propagating through a zonally uniform atmosphere, the wave action flux (wave action times vertical group velocity C_{gz}) is proportional to the momentum flux,

$$AC_{gz} = \frac{\overline{\rho u'w'}}{k}. \tag{1}$$

Perturbations (denoted with primes) are related to amplitudes (denoted with tilde) as $T' = \tilde{T}e^{i\phi}$ where ϕ is phase. Polarization relations for the Kelvin wave can be used to relate the momentum flux to the Kelvin wave temperature amplitude $\tilde{T}$. From the thermodynamic equation we can relate vertical velocity and temperature perturbations,

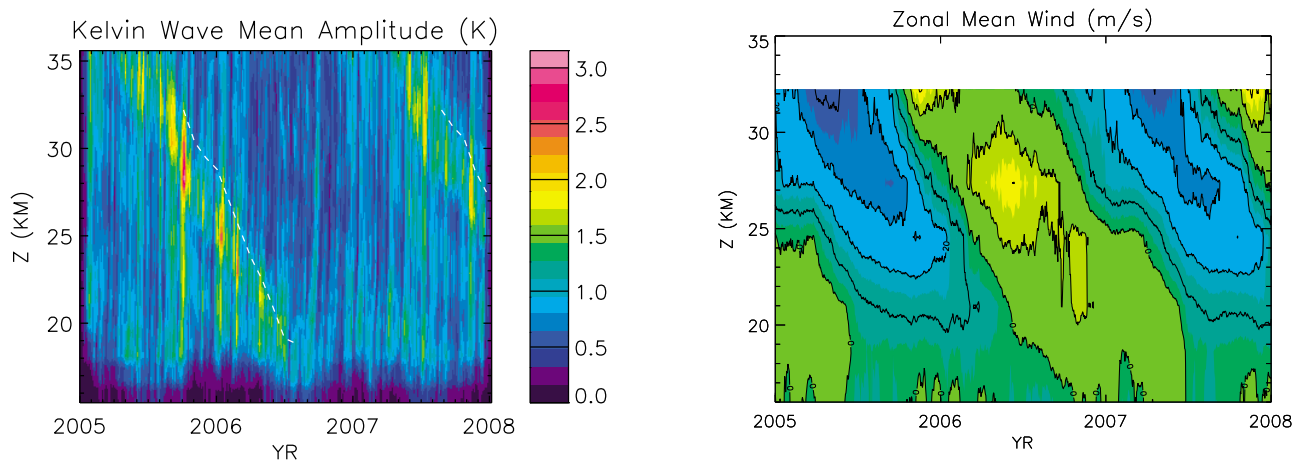$$w' = \frac{ig\hat{\omega}}{N^2}\frac{T'}{\overline{T}}, \tag{2}$$

Figure 7. (left) Kelvin wave temperature amplitudes as a function of time and height at the equator. The dashed white lines show the descent of the zero wind contour below the westerly wind phase with time. Kelvin wave amplitudes tend to peak below these lines. (right) Zonal mean winds on the equator taken from the NCEP reanalysis for this same period. The contour interval is 10 m s^{-1}.

and horizontal wind perturbations can be related to vertical wind perturbations via continuity,

$$u' = \frac{-m}{k} w'. \qquad (3)$$

Here $\overline{\rho}$ is the zonal mean' density, g is gravitational acceleration, $\hat{\omega} = \omega - kU$ is the intrinsic frequency, and N is the buoyancy frequency. Then using the Kelvin wave dispersion relation $\hat{\omega}/N = -k/m$,

$$AC_{gz} = \frac{\overline{\rho}g^2}{2k} \frac{\hat{\omega}}{N^3} \left(\frac{\tilde{T}}{\overline{T}}\right)^2 \qquad (4)$$

If we assume A is constant in time, then at any one altitude, the variations in Kelvin wave amplitude with time will be governed by

$$\frac{\tilde{T}}{\overline{T}} \propto \left(\frac{C_{gz}N^3}{\hat{\omega}}\right)^{1/2} = \left(\frac{\hat{\omega}N^2}{k}\right)^{1/2}, \qquad (5)$$

where the final equality uses $C_{gz} = \hat{\omega}/m$ and the dispersion relation. At altitudes in the TTL between 13 and 18 km, the variations in (5) show a clear annual cycle with phase that matches the observed Kelvin wave amplitudes in the TTL. Figure 6 (bottom) shows the results of (5) normalized by the minimum in the time series at 16 km using observed winds and stability and for two Kelvin waves with phase speeds 10 m s^{-1} (solid line) and 25 m s^{-1} (dashed line). The variation in time is dominated by variations in N with a secondary contribution from $\hat{\omega}$. The latter effect means the variations are more exaggerated for slower phase speed Kelvin waves. The result illustrates that variations in energy flux and potential energy associated solely with variations in the background winds and static stability could largely explain the observed annual cycle in Kelvin wave temperature amplitudes in the TTL. Note that at lower altitudes, the time variations given by (5) are very weak, and at altitudes above 18 km, the variations have a QBO time scale.

[18] For completeness, we also examined whether a seasonal change in the latitudinal scale (L_y) of the Kelvin waves might cause the seasonal variation in Kelvin wave amplitudes we observe on the equator. Following *Hitchman and Leovy* [1988], $L_y \propto \hat{\omega}^{1/2}$. As L_y shrinks, the amplitude on the equator is expected to grow [*Hitchman and Leovy*, 1988]. However, seasonal variations in temperature amplitude due to these changes in L_y are relatively small near the tropopause, and are opposite in phase to the observed cycle in Kelvin wave temperature amplitude, so this effect cannot explain the observed annual cycle in the TTL.

[19] The local Kelvin wave amplitudes shown in Figure 5 that reach ±2 K at 16 km during the boreal summer months are similar to observed temperature oscillations affecting cirrus cloud formation [*Boehm and Verlinde*, 2000]. The annual cycle in the Kelvin wave temperature oscillations also therefore suggests a possible annual cycle in Kelvin wave cirrus cloud effects.

4.2. Interannual Cycle in the Lower Stratosphere

[20] The interannual cycle in Kelvin waves above 20 km is illustrated in the time-height plot of amplitudes on the equator shown in Figure 7. The solid lines mark the descent of the zero wind line where the QBO shifts from easterly to westerly. Kelvin wave amplitudes are largest just below this line and decrease rapidly above it. This is an expected pattern if Kelvin waves are driving the descent of the QBO westerly winds with time. Similar interannual patterns following the descent of westerly winds appear in analyses of SABER data [*Ern et al.*, 2008], although different in detail. *Randel and Wu* [2005] analyzed 14 months of CHAMP and SAC-C GPS temperature data, isolating Kelvin waves with $k = 1$–2. Their results show a peak in Kelvin waves near the tropopause in the December–January–February months. They also examined the "residual temperature variance" that had shorter scales with $k > 2$. This residual shows qualitatively similar patterns to our $k = 1$–5 Kelvin wave signal, suggesting that at least some of their residual is likely due to higher wave number Kelvin waves.
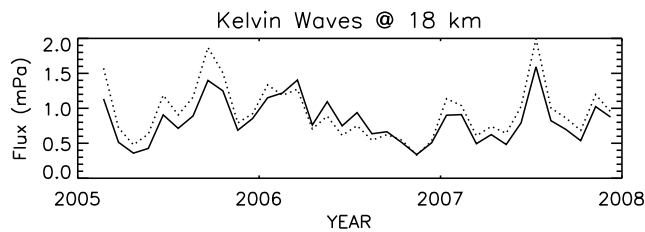
Figure 8. Comparison of two methods for computing Kelvin wave momentum fluxes at 18 km altitude. Both methods compute the flux from the observed temperatures and Fourier analyzed k using (6). The dotted line uses a wavelet method to determine $m(z)$ while the solid line uses the dispersion relation (7) to compute $m(z)$ using the Fourier analyzed ω and NCEP zonal winds.

4.3. Kelvin Wave Momentum Fluxes and Mean Flow Forcing

[21] We next compute Kelvin wave momentum fluxes throughout the HIRDLS observation period and examine their role in driving the QBO. Momentum flux can be estimated directly from the HIRDLS temperature measurements with

$$M = \frac{\rho}{2} \frac{k}{m} \left(\frac{g\tilde{T}}{N\overline{\overline{T}}} \right)^2. \qquad (6)$$

Written in this form, all terms in the equation can be derived directly from the HIRDLS measurements. Kelvin wave modes are isolated as a function of ω and k using the Salby method. This defines the monthly averaged temperature amplitude as a function of wave number and frequency and height $\tilde{T}(k, \omega, z)$ for each mode resolved in the Kelvin wave band. The vertical structure m is estimated with two methods. In the first method, we compute the vertical variation in vertical wave number $m(z)$ for each mode using an S-transform wavelet-type analysis, and estimate momentum flux with (6). In the second method, we estimate $m(z)$ using the Kelvin wave dispersion relation,

$$m(z) = N(z)k/(\omega - U(z)k), \qquad (7)$$

where $U(z)$ is the zonal wind and $N(z)$ is the buoyancy frequency. This second method requires supplementary wind information, that we get from the zonal mean of the NCEP reanalysis. The result gives monthly mean momentum flux as a function of height and time. In both cases, results are averaged over 5°S–5°N latitudes. We also compute the force on the mean flow F, which is related to the vertical derivative of the flux,

$$F = \frac{-1}{\rho} \frac{\partial M}{\partial z}. \qquad (8)$$

[22] Momentum fluxes derived from the two different methods are compared in Figure 8 at an altitude of 18 km, just above the tropopause. The results of both methods are very similar, and differ by ~20%. The force profiles derived from the wavelet method, however, suffer from spectral resolution

limitations. These give sudden jumps in $m(z)$ and also $M(z)$ (via (6)), so the derivative in (8) shows artificial peaks wherever m jumps from one value to another. The use of (7) on the other hand gives more smoothly varying flux profiles that appear more realistic. We subsequently use this second method, using (7) to compute $m(z)$ for both the fluxes and the mean flow forcing. The results are shown as a function of time and height in Figure 9. This is similar to the method used in SABER Kelvin wave momentum flux estimates [*Ern and Preusse*, 2009]. Our momentum fluxes appear to be somewhat larger than reported in the SABER analysis, possibly because the improved vertical resolution of HIRDLS may allow us to see more of the spectrum. The improved vertical resolution along with the HIRDLS cloud detection product [*Massie et al.*, 2007] also allows us to study Kelvin waves at lower altitudes, closer to the tropopause, where the fluxes are larger.

4.4. Kelvin Wave Forcing of the QBO

[23] The momentum fluxes in Figure 9 show dramatic decreases with height as the waves approach the zero wind line associated with the descending westerly winds with time (dashed lines in Figure 9). From (8), the force (Figure 9, bottom) correspondingly shows Kelvin wave participation in driving the descent of the westerly wind phase of the QBO. The force is only very weak or absent during peak westerly winds as expected from theoretical understanding of the wave driving of the QBO [*Plumb*, 1977; *Holton and Lindzen*, 1972]. We compute the fractional contribution of Kelvin waves observed with HIRDLS to driving the QBO wind acceleration at the equator. The total force is estimated using a one-dimensional approach suitable for Kelvin waves as the sum of the observed zonal wind acceleration $\partial U/\partial t$ and the vertical advection of the wind $\overline{w}* \; \partial U/\partial z$ and shown in
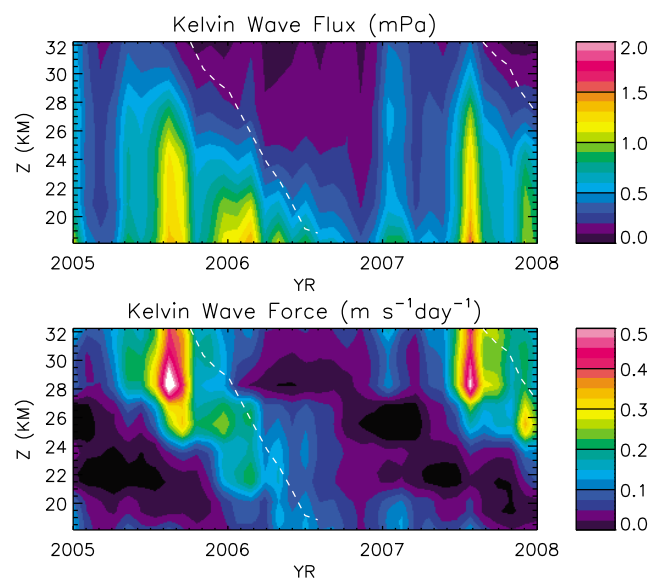

Figure 9. (top) Time-height changes in Kelvin wave momentum flux and (bottom) the force on the mean flow due to dissipation of this flux. The dashed white lines show the zero wind line associated with descending westerly winds in this altitude region where the QBO dominates the circulation.
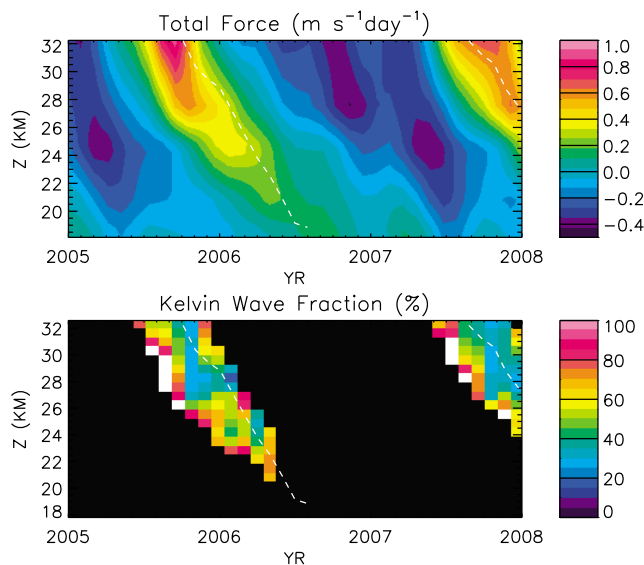
Figure 10. (top) Time-height changes in the total force required to drive the QBO and (bottom) the fraction of this force contributed by Kelvin waves observed with HIRDLS. The fraction is only computed in regions where the total force exceeds 0.2 m s^{-1} d^{-1}. The dashed white lines are again zero wind lines as in Figure 9.

Figure 10 (top). U is the monthly mean zonal mean wind as defined by the NCEP reanalysis, and $\overline{w}*$ is the vertical component of the transformed Eulerian mean meridional circulation in the tropics [Andrews et al., 1987]. We neglect other terms in the total force, including meridional advection (because the QBO wind is approximately symmetric about the equator) and the Coriolis force (which vanishes at the equator). We adopt a profile of $\overline{w}*$ based on work by Schoeberl et al. [2008] as given in Table 1. We neglect any seasonal variations in $\overline{w}*$, which are small compared to the uncertainties [Schoeberl et al., 2008]. The acceleration term and vertical advection term are comparable in magnitude, although the advection term becomes more important in the middle stratosphere than in the lower stratosphere.

[24] We next compute the ratio of the Kelvin wave force to the total force wherever the total force exceeds 0.2 m s^{-1} d^{-1}. In other regions the total force in the denominator can become too small leading to erroneously high fractions. The fraction is shown in Figure 10 (bottom). An average value at all heights 18–32 km and times when the total force exceeds 0.2 m s^{-1} d^{-1} (excluding fractions > 100%) is 47%. Changing the threshold for total force from 0.1–0.25 m s^{-1} d^{-1} gives a range of 44–49%. This fraction lies at the upper end of the range estimated for all equatorial waves in the westerly phase of the QBO in the Kawatani et al. [2010] model study. It is difficult to compare directly to the fractional QBO forcing reported by Ern and Preusse [2009], but certainly our results appear very similar at times. The HIRDLS 5°S–5°N fractional forcing tends to be larger than the SABER 10°S–10°N forcing at times and heights close to the zero wind line during descending westerlies. This could be partly due to resolution: The finer HIRDLS vertical resolution will allow observation of Kelvin waves at shorter vertical wavelengths, which will occur under conditions of descending westerly winds. Our result is however in general agreement with all of these and

other earlier studies, that Kelvin waves are responsible for roughly half of the forcing during the descent of the QBO westerly phase.

5. Conclusions

[25] We have shown results of an asynoptic Fourier analysis of HIRDLS temperatures in the tropics, and demonstrated the ability of HIRDLS to resolve fine structure of equatorial waves in both latitude and height. Vertical wavelengths as short as 4 km can be clearly observed. These short vertical wavelength waves are particularly visible in the lower stratosphere at times and altitudes when the QBO winds Doppler shift and refract the waves to low intrinsic frequencies and high vertical wave numbers. MRG waves, ER waves, and Kelvin waves are clearly resolved in the $k - \omega$ temperature spectrum at k and ω regions of the spectrum identified by their dispersion relations [Matsuno, 1966]. The theoretical latitude and height structures of these waves appear very clearly in the data despite the fact that the analysis is carried out independently at each 2.5° latitude bin and height resolved by HIRDLS. Power at inertia-gravity wave frequencies is weak but also evident in the spectra.

[26] Kelvin waves form the strongest signal in the data throughout the 3 year data record. We identify an annual cycle in the temperature amplitudes of Kelvin waves at altitudes in the TTL (~15–18 km). Temperature amplitudes vary annually by a factor of 2 or more at 16 km altitude, where cold anomalies as large as 2K are observed in boreal summer-to-fall months (~May to October). These temperature anomalies are cold enough to affect cirrus formation. Possible causes of the annual cycle are investigated. Annual changes in zonal mean wind (U) and static stability (N) can lead to an annual cycle in Kelvin wave potential energy with the same phase as seen in the observations, and with amplitude variations that are largest for slow Kelvin waves. These effects of the background atmosphere on wave propagation may be the primary cause of the annual cycle in temperature amplitudes. Loss of data due to the presence of high cirrus clouds also has an annual cycle, with peak losses in the cold tropopause conditions during boreal winter, which leads to enhanced noise during this season. If these cirrus occur primarily within the largest Kelvin wave cold anomalies, it is possible that data loss may selectively remove measurements with largest Kelvin wave amplitudes. We cannot investigate this possibility further using HIRDLS data alone, but future investigations with GPS measurements may be able to resolve this question. GPS temperature retrievals are influenced by water vapor but are not sensitive to clouds and so should have fewer such problems at TTL altitudes.

[27] We also examine an interannual cycle in Kelvin waves observed in the stratosphere between 20 and 35 km. A

Table 1. Vertical Velocity Profile[a]

Altitude (km)	$\overline{w}*$ (cm s^{-1})
16.1	0.039
18.6	0.031
21.0	0.028
24.5	0.043
27.4	0.058
32.2	0.071

[a]Based on Figure 7 of Schoeberl et al. [2008].

descending peak in amplitudes in time following the zero wind line of descending QBO westerlies appears very similar to the analysis of Kelvin waves in SABER temperatures [*Ern and Preusse*, 2009] and to the "residual temperature variance" (due to *k* higher than 2) in the *Randel and Wu* [2005] GPS analysis. We analyze this as a signal of Kelvin wave forcing of the descent of QBO westerlies, and compute momentum fluxes and mean flow force due to Kelvin waves, similarly to *Ern and Preusse* [2009], but using the higher-resolution HIRDLS data. Kelvin waves contribute on average ~47% of the total wave forcing during the descent of the QBO westerly phase at altitudes between 18 and 32 km, a fraction that is near the upper end or comparable to other recent estimates [*Ern and Preusse*, 2009; *Kawatani et al.*, 2010]. Although differences in detail would likely be apparent in one-to-one comparisons, particularly as Kelvin waves are refracted to short vertical wavelength in descending westerly winds, our estimates are in general agreement with other earlier studies that have concluded that Kelvin waves are responsible for roughly half of the forcing of the QBO westerly phase.

[28] We have also examined the common assumption that the vertical wave number *m* can be computed from the dispersion relation (7) using observed ω and k and auxiliary wind data. The comparison of Kelvin wave momentum fluxes using observed and calculated *m* shown in Figure 8 suggests the two methods give very similar results. However the fine structure of the vertical profile of the flux, and therefore the force via (8), differed in detail because of the limited spectral resolution of the wavelet analysis we used to derive *m* directly from the wave vertical structure.

[29] Our results have generally shown that the high vertical and latitudinal resolution of HIRDLS allow a clearer view of the properties of equatorial waves in the upper troposphere and stratosphere, and their interactions with QBO winds, than previous satellite measurements.

References

Alexander, S. P., T. Tsuda, Y. Kawatani, and M. Takahashi (2008), Global distribution of atmospheric waves in the equatorial upper troposphere and lower stratosphere: COSMIC observations of wave mean flow interactions, *J. Geophys. Res.*, 113, D24115, doi:10.1029/2008JD010039.

Andrews, D., J. Holton, and C. Leovy (1987), *Middle Atmosphere Dynamics*, 489 pp., Academic, San Diego, Calif.

Boehm, M., and S. Lee (2003), The implications of tropical Rossby waves for tropical tropopause cirrus formation and for the equatorial upwelling of the Brewer-Dobson circulation, *J. Atmos. Sci.*, 60, 247–261.

Boehm, M., and J. Verlinde (2000), Stratospheric influence on upper tropospheric tropical cirrus, *Geophys. Res. Lett.*, 27(19), 3209–3212.

Canziani, P. O., J. R. Holton, E. G. Fishbein, L. Froidevaux, and J. W. Waters (1994), Equatorial Kelvin waves: A UARS MLS view, *J. Atmos. Sci.*, 51, 3053–3076.

Canziani, P. O., J. R. Holton, E. G. Fishbein, and L. Froidevaux (1995), Equatorial Kelvin wave variability during 1992 and 1993, *J. Geophys. Res.*, 100(D3), 5193–5202.

Cho, H.-K., K. P. Bowman, and G. R. North (2004), Equatorial waves including the Madden-Julian oscillation in TRMM rainfall and OLR data, *J. Clim.*, 17, 4387–4406.

Ern, M., and P. Preusse (2009), Wave fluxes of equatorial Kelvin waves and QBO zonal wind forcing derived from SABER and ECMWF temperature space-time spectra, *Atmos. Chem. Phys.*, 9, 3957–3986.

Ern, M., P. Preusse, M. Krebsbach, M. G. Mlynczak, and J. M. Russell III (2008), Equatorial wave analysis from SABER and ECMWF temperatures, *Atmos. Chem. Phys.*, 8, 845–869.

Fueglistaler, S., A. E. Dessler, T. J. Dunkerton, I. Folkins, Q. Fu, and P. W. Mote (2009), Tropical tropopause layer, *Rev. Geophys.*, 47, RG1004, doi:10.1029/2008RG000267.

Fujiwara, M., et al. (2009), Cirrus observations in the tropical tropopause layer over the western Pacific, *J. Geophys. Res.*, 114, D09304, doi:10.1029/2008JD011040.

Garcia, R., T. Dunkerton, R. Lieberman, and R. Vincent (1997), Climatology of the semiannual oscillation of the tropical middle atmosphere, *J. Geophys. Res.*, 102(D22), 26,019–26,032.

Gille, J. C., et al. (2008), The High Resolution Dynamics Limb Sounder (HIRDLS): Experiment overview, recovery, and validation of initial temperature data, *J. Geophys. Res.*, 113, D16S43, doi:10.1029/2007JD008824.

Giorgetta, M. A., E. Manzini, and E. Roeckner (2002), Forcing of the quasi-biennial oscillation from a broad spectrum of atmospheric waves, *Geophys. Res. Lett.*, 29(8), 1245, doi:10.1029/2002GL014756.

Hitchman, M. H., and C. B. Leovy (1988), Estimation of the Kelvin wave contribution to the semiannual oscillation, *J. Atmos. Sci.*, 45, 1462–1475.

Holton, J. R. (1972), Waves in the equatorial stratosphere generated by tropospheric heat sources, *J. Atmos. Sci.*, 29, 368–375.

Holton, J. R., and R. S. Lindzen (1972), An updated theory for the quasi-biennial cycle of the tropical stratosphere, *J. Atmos. Sci.*, 29, 1076–1080.

Holton, J., M. Alexander, and M. Boehm (2001), Evidence for short vertical wavelength Kelvin waves in the DOE-ARM Nauru99 radiosonde data, *J. Geophys. Res.*, 106(D17), 20,125–20,129.

Jensen, E., and L. Pfister (2004), Transport and freeze drying in the tropical tropopause layer, *J. Geophys. Res.*, 109, D02207, doi:10.1029/2003JD004022.

Kawatani, Y., K. Sato, T. J. Dunkerton, S. Watanabe, S. Miyahara, and M. Takahashi (2010), The roles of equatorial trapped waves and internal inertia-gravity waves in driving the quasi-biennial oscillation. Part I: Zonal mean wave forcing, *J. Atmos. Sci.*, 67, 963–980, doi:10.1175/2009JAS3222.1.

Kiladis, G. N., M. C. Wheeler, P. T. Haertel, K. H. Straub, and P. E. Roundy (2009), Convectively coupled equatorial waves, *Rev. Geophys.*, 47, RG2003, doi:10.1029/2008RG000266.

Liebmann, B., and C. A. Smith (1996), Description of a complete (interpolated) outgoing longwave radiation dataset, *Bull. Am. Meteorol. Soc.*, 77, 1275–1277.

Madden, R., and P. Julian (1994), Observations of the 40–50-day tropical Oscillation—A review, *Mon. Weather Rev.*, 122, 814–837.

Massie, S., et al. (2007), High Resolution Dynamics Limb Sounder observations of polar stratospheric clouds and subvisible cirrus, *J. Geophys. Res.*, 112, D24S31, doi:10.1029/2007JD008788.

Massie, S., J. Gille, C. Craig, R. Khosravi, J. Barnett, W. Read, and D. Winker (2010), HIRDLS and CALIPSO observations of tropical cirrus, *J. Geophys. Res.*, 115, D00H11, doi:10.1029/2009JD012100.

Masunaga, H. (2007), Seasonality and regionality of the Madden-Julian Oscillation, Kelvin wave, and equatorial Rossby wave, *J. Atmos. Sci.*, 64, 4400–4416.

Matsuno, T. (1966), Quasi-geostrophic motions in the equatorial area, *J. Meteorol. Soc. Jpn.*, 44, 25–43.

Meehl, G. A. (1987), The annual cycle and interannual variability in the tropical Pacific and Indian Ocean regions, *Mon. Weather Rev.*, 115, 27–50.

Mitchell, T. P., and J. M. Wallace (1992), The annual cycle in equatorial convection and sea surface temperature, *J. Clim.*, 5, 1140–1156.

Norton, W. A. (2006), Tropical wave driving of the annual cycle in tropical tropopause temperatures. Part II: Model results, *J. Atmos. Sci.*, 63, 1420–1431.

Plumb, R. A. (1977), The interaction of two internal waves with the mean flow: Implications for the theory of the quasi-biennial oscillation, *J. Atmos. Sci.*, 34, 1847–1858.

Randel, W. J., and F. Wu (2005), Kelvin wave variability near the equatorial tropopause observed in GPS radio occultation measurements, *J. Geophys. Res.*, 110, D03102, doi:10.1029/2004JD005006.

Ryu, J.-H., and S. Lee (2010), Effect of tropical waves on the tropical tropopause-transition-layer upwelling, *J. Atmos. Sci.*, 67, 3130–3148.

Ryu, J.-H., S. Lee, and W.-W. Son (2008), Vertically propagating Kelvin waves and tropical tropopause variability, *J. Atmos. Sci.*, 65, 1817–1837, doi:10.1175/2007JAS2466.1.

Salby, M. (1982), Sampling theory for asynoptic satellite observations. Part I: Space-time spectra, resolution, and aliasing, *J. Atmos. Sci.*, 39, 2577–2600.

Salby, M., D. L. Hartmann, P. L. Bailey, and J. C. Gille (1984), Evidence for equatorial Kelvin modes in NIMBUS-7 LIMS, *J. Atmos. Sci.*, 41, 220–235.

Sassi, F., and R. Garcia (1997), The role of equatorial waves forced by convection in the tropical semiannual oscillation, *J. Atmos. Sci.*, *54*, 1925–1942.

Schoeberl, M. R., A. R. Douglass, R. S. Stolarski, S. Pawson, S. E. Strahan, and W. Read (2008), Comparison of lower stratospheric tropical mean vertical velocities, *J. Geophys. Res.*, *113*, D24109, doi:10.1029/2008JD010221.

Shiotani, M., J. C. Gille, and A. E. Roche (1997), Kelvin waves in the equatorial lower stratosphere as revealed by Cryogenic Limb Array Etalon Spectrometer temperature data, *J. Geophys. Res.*, *102*(D22), 26,131–26,140.

Srikanth, R., and D. A. Ortland (1998), Analysis of Kelvin waves in High-Resolution Doppler Imager and Microwave Limb Sounder stratosphere measurements using a constrained least squares method, *J. Geophys. Res.*, *103*(D18), 23,131–23,151.

Tsai, J.-F., T. Tsuda, G. Hajj, J. Wickert, and Y. Aoyama (2004), Equatorial Kelvin waves observed with GPS occultation measurements (CHAMP and SAC-C), *J. Meteorol. Soc. Jpn.*, *82*, 397–406.

Tsuda, T., Y. Murayama, H. Wiryosumarto, S. W. B. Harijono, and S. Kato (1994), Radiosonde observations of equatorial atmosphere dynamics over Indonesia: 1. Equatorial waves and diurnal tides, *J. Geophys. Res.*, *99*(D5), 10,491–10,506.

Wheeler, M., and G. Kiladis (1999), Convectively-coupled equatorial waves: Analysis of clouds and temperature in the wavenumber-frequency domain, *J. Atmos. Sci.*, *56*, 374–399.

M. J. Alexander, CoRA Division/NorthWest Research Associates, 3380 Mitchell Ln., Boulder, CO 80301, USA. (alexand@cora.nwra.com)

D. A. Ortland, Seattle Division/NorthWest Research Associates, Redmond, WA 98052, USA.